

Supplement of Hydrol. Earth Syst. Sci., 23, 1751–1762, 2019  
<https://doi.org/10.5194/hess-23-1751-2019-supplement>  
© Author(s) 2019. This work is distributed under  
the Creative Commons Attribution 4.0 License.



*Supplement of*

## **The El Niño event of 2015–2016: climate anomalies and their impact on groundwater resources in East and Southern Africa**

**Seshagiri Rao Kolusu et al.**

*Correspondence to:* Seshagiri Rao Kolusu (s.kolusu@sussex.ac.uk, seshukolusu@gmail.com)

The copyright of individual parts of the supplement might differ from the CC BY 4.0 License.

---

24 **Supplementary Information**

25

26 S1. Climatological context: El Niño and other drivers of climate over EASE/SA, the 2015-16

27 El Niño event and climate anomalies over SA

28

29 The climatological mean austral summer wet season of October-April rainfall (Fig. S1(a))

30 shows a maximum extending Northwest-Southeast from Democratic Republic of Congo

31 (DRC)/Angola in the west, across Zambia, Malawi to northern Mozambique in the East. The

32 leading mode of interannual variability in rainfall and SPEI-7, is a north/south dipole pattern

33 of opposing anomalies across EASE and SA, with a divide at  $\sim 11^{\circ}\text{S}$ , the approximate mean  
34 latitude of rainfall maximum and is strongly related to ENSO. This structure clearly evidenced  
35 by the leading Empirical Orthogonal Function (EOF) of SPEI-7 (Fig. S1(b)) which explains  
36 21.5% of total variance. The time coefficients correlate strongly with tropical SSTs (Fig. S1(d))  
37 highly characteristic of the ENSO SST anomalies in both the Pacific and Indian Oceans,  
38 notably the SW/NE positive/negative correlation dipole across the southwest/equatorial Indian  
39 Ocean (e.g. Lindesay, 1988; Reason *et al.*, 2000, Lazenby *et al.*, 2016). As such, for Africa  
40 South of the equator the leading mode of climate variability is strongly related to ENSO, with  
41 wet (dry) anomalies during El Niño (la Niña) events across EASE (SA). The EOF pattern is  
42 largely insensitive to the length of choice of months in the wet season. This north-south dipole  
43 response across EASE/SA to ENSO has been well documented previously (Ropelewski and  
44 Halpert, 1987; Janowiak, 1988; Goddard and Graham, 1999; Manatsa *et al.*, 2011), although  
45 the physical mechanisms of teleconnection remain elusive (see Blamey *et al.* 2018 for a  
46 summary).

47

48 The climate anomaly pattern during 2015-16 was highly characteristic of this mode (compare  
49 Figs. 1(a) and S1b). Very strong SST anomalies over the Pacific and elsewhere in the tropics  
50 during 2015-16 (Fig. S1(d)) were associated with a strong north/south dipole in rainfall with  
51 drought in SA (Fig. 1(a)). The socio-economic impacts were pronounced, with much of SA  
52 affected by drought, leading to a regional drought disaster declaration by the Southern Africa  
53 Development Community (SADC). By September 2016, six SADC countries had declared  
54 ‘national drought emergencies’ (Botswana, Namibia Lesotho, Malawi, Swaziland and  
55 Zimbabwe) with drought emergency declared for seven of the South Africa’s nine provinces,  
56 and a temporary red alert also declared for central and Southern provinces of Mozambique  
57 (SADC 2016a). The drought resulted in an extensive loss of crops and livestock, an increase in  
58 food prices, driving an estimated 39 million people into deeper food insecurity (SADC 2016a;  
59 2016b; Archer *et al.*, 2017). Surface water shortages further affected electricity generation and  
60 domestic supply, affecting economic activity and human health (SADC, 2016a; Siderius *et al.*  
61 2018).

62

63 The 2015-16 El Niño was without doubt one of the strongest on record, and by some  
64 indicators was actually the strongest. There are many measures of ENSO strength (see

65 e.g. <https://www.esrl.noaa.gov/psd/enso/dashboard.html>), which provide a mixed picture on  
66 the relative strength of the major events. 2015-16 appears strongest based on the Niño 3.4,  
67 Niño 4 and Bivariate El Niño – Southern Oscillation index, whilst 1997-98 is the strongest  
68 based on the (East pacific Niño 3 and 1+2 SST indices, east Pacific heat content and the  
69 Multivariate El Niño index. However, 2015-16 was certainly more persistent than 1997-98  
70 with many indices turning positive at some time in 2014 related to the El Niño event that was  
71 predicted in 2014 but did not develop fully until 2015-16 (Levine and McPhaden, 2016).

72

73 However, there is substantial diversity in the character of El Niño events, in terms of both (i)  
74 the structure and magnitude of anomalies in the Pacific sector. For example, 2015-16 and 1997-  
75 98 differed in that the former was stronger in the Central Pacific sector (Niño3.4 and Niño SST  
76 region) and the latter in the East Pacific (Niño 1+2 and Niño 3 SST regions) (ii) the state and  
77 evolution of other regional drivers of climate variability which interact with ENSO  
78 teleconnection processes, such that the remote impacts over Africa can be quite variable (e.g.  
79 Ratnam *et al.*, 2014; Preethi *et al.*, 2015, Hoell *et al.*, 2017; Blamey *et al.*, 2018). Across  
80 Southern Africa (SA) multiple regional structures of ocean and atmospheric variability  
81 modulate the impacts of ENSO including the South Indian Ocean dipole (Reason, 2001) as  
82 well as the Angola low and Botswana High atmospheric features (Blamey *et al.*, 2018).  
83 Furthermore, intraseasonal variability associated with the Madden Julian Oscillation, with 30-  
84 60 day timescales can also modulate interannual drivers of variability, particularly over East  
85 Africa (Berhane and Zaitchik, 2014).

86

87 Over East Africa rainfall is more strongly related to the state of the Indian Ocean than to ENSO.  
88 The Indian Ocean Zonal mode (IOZM), an east-west pattern of atmosphere-ocean variability  
89 across the Equatorial Indian ocean, strongly modulates the regional Walker circulation and  
90 hence rainfall over East Africa. During positive IOZM events warmer ocean temperatures in  
91 the equatorial west Indian Ocean and cooler temperatures in the east lead to enhanced rainfall  
92 over EASE, with negative IOZM leading to a reduction in rainfall (see Nicholson 2017 for a  
93 review and references therein). The impact of ENSO on EASE is therefore intimately  
94 connected to the state of the IOZM (Black *et al.*, 2003, Manatsa *et al.*, 2011). During 2015-16  
95 the IOZM was only weakly positive (see SST anomalies in Fig. S1(d)) and the seasonal de-  
96 trended IOZM index (Saji *et al.*, 1999) in 2015-16 was ranked 16<sup>th</sup> out of 150 years. As a result,

97 the mean equatorial zonal Indian Ocean Walker cell with ascent (descent) in the east at  $\sim 100^{\circ}\text{E}$   
98 (west at  $\sim 50^{\circ}\text{E}$ ) of the basin is only weakly perturbed. The zonal cross section over the East  
99 Africa-Indian Ocean sector indicates that enhanced large-scale uplift is limited to a quite  
100 restricted region of EASE from  $\sim 33^{\circ}$ - $40^{\circ}\text{E}$ . In this way, the weak reorganisation of the Indian  
101 ocean Walker circulation led to rather moderate rainfall anomalies over EASE (Section 3.1).

102

## 103 S2. SPEI-7 Intensity-Area-Frequency (IAF) curves and associated return period estimates, and 104 attribution of anthropogenic influence on the SA drought 2015-16

105

106 Droughts are spatially extensive but variable features. We represent the spatial extent using  
107 IAF curves which show the intensity of SPEI-7 water balance anomalies across all spatial scales  
108 within a study domain. IAF curves are independent of the precise spatial patterns of SPEI-7  
109 anomalies, and as such allow us to compare droughts between individual years, and to calculate  
110 the return periods for drought events across scales. This direct comparability of SPEI-7 IAF  
111 curves is valuable since no two drought events have exactly the same spatial pattern. The IAF  
112 curves are derived using the method of Mishra and Cherkauer (2010) separately over the two  
113 study domains of EASE and SA, by calculating the mean SPEI-7 value of grid cells lying within  
114 various areal extent intervals: The areas covered by the lowest (for SA) or highest (for EASE)  
115 5th, 10th, 20th...100th areal percentiles of SPEI grid cell values within the domain area i.e.  
116 when all grid cells are ranked. This allows, for each season, the mean SPEI-7 IAF curve to be  
117 plotted (see Fig. 3).

118

119 We then estimate the return period of the 2015-16 El Niño event by comparing the observed  
120 SPEI-7 IAF curve of 2015-16 with IAF curves representing various ‘benchmark’ return  
121 periods (Fig. 3) and finding the closest match, by least squared error. Estimating these  
122 benchmark return periods of drought events is challenging given the relatively short  
123 observational record for what are relatively long duration events, and indeed because of non-  
124 stationarity in climate records under a changing climate. We address both these challenges in  
125 our approach. To counter the problem of insufficient sampling of the extreme tail of the  
126 distribution, we increase our sample of climate events beyond the observed record using large  
127 ensembles of climate model simulations from the HAPPI experiment (Mitchell *et al.*, 2017).  
128 HAPPI is designed specifically to quantify climate extremes, through the use of relatively

129 high model resolution and large initial-condition ensembles. We use precipitation data from  
130 four atmospheric models, namely HadGEM3, CAM5, MIROC5 and NorESM, (degraded to  
131 common resolution of 1°) each with 10 ensemble members, run over the period ~1950s-  
132 2010s, forced with observed SSTs and ‘historical’ greenhouse gases and aerosol radiative  
133 forcings. These simulations provide about 2400 years of simulated data, with greater  
134 statistical definition of the extreme tail of the distribution required for the extreme events,  
135 notably the 2015-16 drought over SA which is the strongest on record. As with the  
136 observations we derive the mean SPEI-7 for each areal extent interval (5th, 10th, etc. spatial  
137 percentiles over the domain), for each of the ~2400 model years. Estimation of return periods  
138 is based on the Extreme Value Theory (EVT), widely used for the description of rare climate  
139 events in the extreme tail of the parameter distribution. The Generalized Extreme Value  
140 distribution (GEV) is fitted to the distribution of only the extreme SPEI-7 values, for each  
141 areal extent separately (using maximum likelihood estimation and a chi-squared goodness-of-  
142 fit test, Coles *et al.*, 2001). This distribution of extremes (‘block maxima’) is composed of the  
143 most intense SPEI-7 values (for drought over the SA domain SPEI-7 is multiplied by -1)  
144 within non-overlapping ‘blocks’ of 30 years, a standard climatological period. Then, return  
145 periods are estimated by inverting the resulting GEV cumulative probability distribution for a  
146 range of periods from 30-300 years, for each areal extent separately, providing IAF curves for  
147 benchmark return periods (see Fig. 3). Whilst our approach is similar to previous drought  
148 analyses (e.g. Robeson, 2015) we recognise a number of caveats. First, the estimated return  
149 periods are sensitive to the arbitrary choice of block size and we estimate the uncertainty  
150 associated with this using periods of 25-60 years. Second, whilst the large ensembles  
151 provided by the HAPPI experiment are designed specifically for analysis of extremes they  
152 necessarily provide only a partial representation of the climate variability ‘space’.

153

154 For estimation of return periods shorter than the duration of one ‘block’ (30 years), we  
155 follow Mishra and Cherkauer (2010) and Philip *et al.* (2018) in fitting a distribution to the  
156 historical record of SPEI-7 data. For each areal extent interval (5<sup>th</sup>, 10<sup>th</sup>, etc. spatial  
157 percentiles) we fit a GEV distribution to the 116 historical SPEI-7 data points. We then invert  
158 the cumulative distribution to derive return periods for every spatial percentile, giving a set of  
159 IAF benchmark return period curves. Finally, we conduct all the above IAF curve return  
160 period analysis using SPEI-7 derived with each of the three PET equations and provide the

161 average return period estimates and the associated range to represent this component of  
162 uncertainty.

163

164 It is likely that anthropogenic climate change is, and will continue to, affect large-scale  
165 hydrology. As such, climate risks are changing and non-stationarity in climate records  
166 complicates the interpretation of return periods. However, the IPCC recent assessment report  
167 concludes that there is only low confidence in detection and attribution of observed changes in  
168 drought extremes globally (Bindoff *et al.*, 2013), largely due to uncertainties in distinguishing  
169 relatively small trends in precipitation from decadal variability, especially given limitations in  
170 precipitation data. Nevertheless, attribution of recent temperature rises is robust even down to  
171 the regional/continental scale (Bindoff *et al.*, 2013). In recent probabilistic event attribution  
172 analyses of tropical drought events the contribution of anthropogenic temperature effects is  
173 discernible, in contrast to that of precipitation (Marthews *et al.*, 2015). As such, the full causal  
174 chain from climate anomaly through water balance to agricultural drought is complex and  
175 typically not well represented in models such that attribution of drought remains extremely  
176 challenging. Therefore, here we estimate the effects purely of anthropogenic temperature trends  
177 on drought risk over SA through a simplified attribution experiment. The SPEI-7 IAF return  
178 period analysis above is repeated, but in deriving the benchmark return period curves the  
179 temperature data, used in calculating PET, has the signal of anthropogenic climate change  
180 removed. Specifically, PET is estimated using the HAPPI multi-ensemble mean temperature  
181 from a counterfactual world without human influence on radiative forcing: the ‘natural’ runs,  
182 in which only the natural forcings (solar variability and volcanic aerosols) are provided to the  
183 models. To ensure space-time consistency in all the climate variables whilst changing the  
184 temperature data, we used the 30-year smoothed temperature from the ‘natural’ model runs to  
185 which is added the anomalies of temperature from the ‘historical’ run with respect to a 30-year  
186 running mean. Not that we derive the SPEI-7 over both datasets merged together so that the  
187 effect of the temperature perturbation between the ‘natural’ and ‘historical’ runs is reflected in  
188 the resulting SPEI-7 values, given that the index is standardised across the timeseries. The  
189 benchmark return period IAF curves are then derived from the SPEI-7 values for each dataset  
190 separately. Thus, comparing the estimated SPEI-7 IAF return periods from the climate with  
191 ‘historical’ temperature with those from a counterfactual climate with the ‘natural’ only  
192 temperature, provides an indication of the influence of the anthropogenic temperature trend

193 effects on drought risk over SA. We note that the SPEI is quite temperature dependent through  
194 PET calculation such that other drought indices may yield different sensitivity to warming.

195

196 We must emphasise that this analysis deliberately considers only the effects of the slowly  
197 evolving anthropogenic influence on temperature. We do not consider anthropogenic  
198 influences on rainfall and the other determinants of PET i.e. wind speed, humidity, radiation  
199 budget, no any changes to variability in temperature or any other variables. Further, the  
200 difference in model estimated temperatures between the ‘natural’ and ‘historical’ run will  
201 include the effects not just of anthropogenic radiative forcing but also the surface energy budget  
202 which itself is affected by precipitation and other near surface variables whose response to  
203 radiative forcing we do not consider. However, in utilising a large model ensemble to define  
204 the statistics of extreme events, we retain some features of the probabilistic event attribution  
205 method (e.g. Allen *et al.*, 2003, Stott *et al.*, 2014) but focus solely on that aspect of climate  
206 change (near surface temperatures) for which we have greatest confidence in the ability of  
207 models to represent with credibility.

208

### 209 S3. Groundwater storage estimates from GRACE and LSMs

210

211 To address uncertainty associated with different GRACE processing strategies to resolve  
212  $\Delta$ TWS (Eq. 1) we apply an ensemble mean of three GRACE TWS. Namely, the CSR land  
213 (version RL05.DSTvSCS1409, Swenson and Wahr, 2006; Landerer and Swenson, 2012) and  
214 JPL Global Mascon (version RL05M\_1.MSCNv01, Watkins *et al.*, 2015; Wiese *et al.*, 2015)  
215 solutions, from NASA’s *GRCTellus* data dissemination site (<http://grace.jpl.nasa.gov/data>),  
216 and a third GRGS GRACE solution (CNES/GRGS release RL03-v1) (Biancale *et al.*, 2006)  
217 from the French Government space agency, Centre National D’études Spatiales (CNES).

218

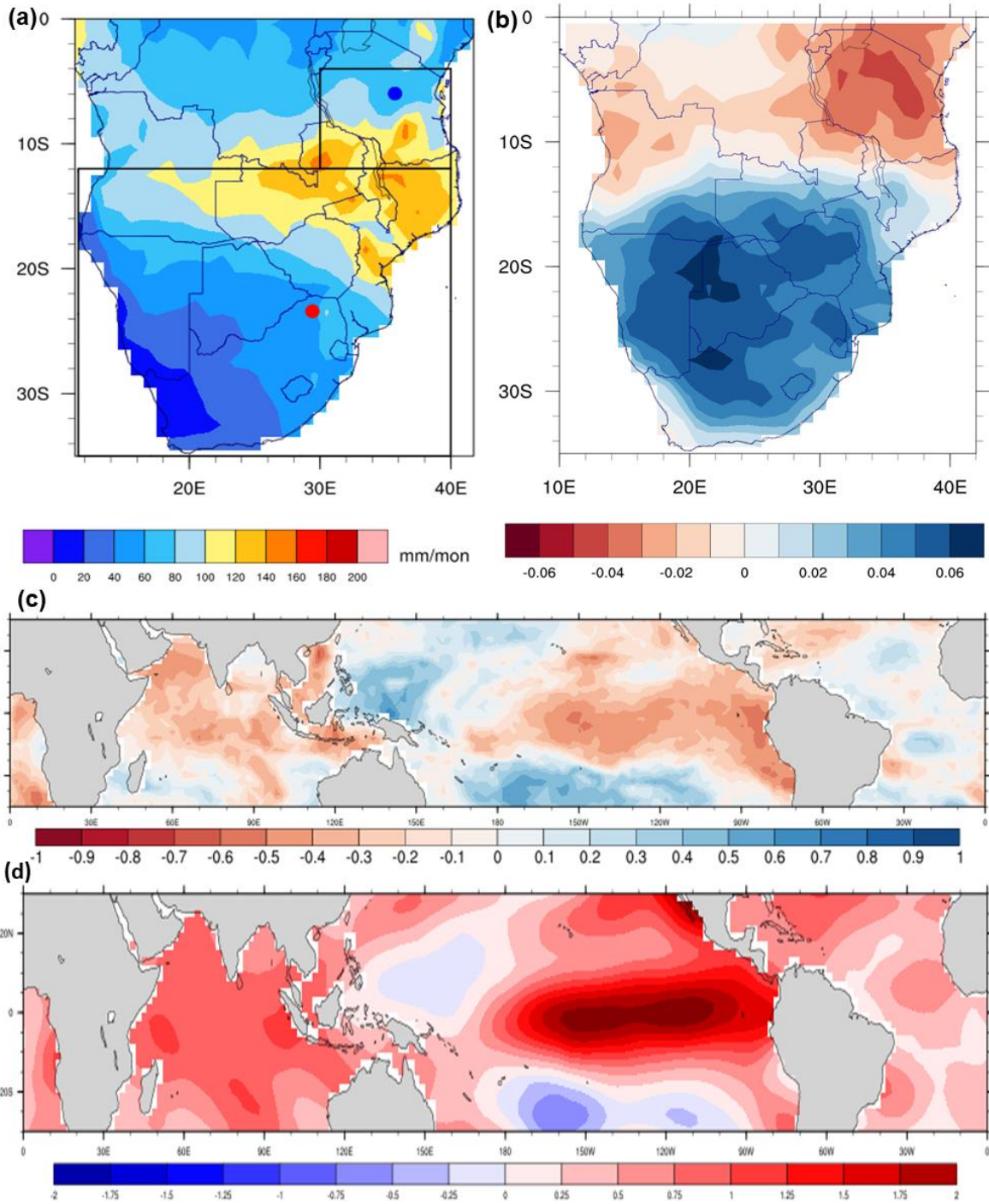
219 *GRCTellus* CSR land solution (version RL05.DSTvSCS1409) is post-processed from spherical  
220 harmonics released by the Centre for Space Research (CSR) at the University of Texas at  
221 Austin. *GRCTellus* gridded datasets are available at a monthly time step and a spatial resolution  
222 of  $1^\circ \times 1^\circ$  (~111 km at equator) though the actual spatial resolution of GRACE footprint is  
223 ~450 km or ~200,000 km<sup>2</sup> (Scanlon *et al.*, 2012). To amplify TWS signals we apply the  
224 dimensionless scaling factors provided as  $1^\circ \times 1^\circ$  bins that are derived from minimising

225 differences between TWS estimated from GRACE and the hydrological fields from the  
226 Community Land Model (CLM4.0) (Landerer and Swenson, 2012). JPL-Mascons (version  
227 RL05M\_1.MSCNv01) data processing involves the same glacial isostatic adjustment  
228 correction but applies no spatial filtering as JPL-RL05M directly relates inter-satellite range-  
229 rate data to mass concentration blocks (mascons) to estimate monthly gravity fields in terms of  
230 equal area  $3^\circ \times 3^\circ$  mass concentration functions in order to minimise measurement errors.  
231 Gridded mascon fields are provided at a spatial sampling of  $0.5^\circ$  in both latitude and longitude  
232 ( $\sim 56$  km at the equator). Similar to *GRCTellus* CSR product, dimensionless scaling factors are  
233 provided as  $0.5^\circ \times 0.5^\circ$  bins (Shamsudduha *et al.*, 2017) that also derive from the Community  
234 Land Model (CLM4.0) (Wiese *et al.*, 2016). The scaling factors are multiplicative coefficients  
235 that minimize the difference between the smoothed and unfiltered monthly  $\Delta$ TWS variations  
236 from the CLM4.0 hydrology model (Wiese *et al.*, 2016). GRGS monthly GRACE products  
237 (version RL03-v1) are processed and made publicly available (<http://grgs.obs-mip.fr/grace>) by  
238 CNES (Shamsudduha *et al.*, 2017). Further details on the Earth's mean gravity-field models  
239 can be found on the CNES official website of GRGS/LAGEOS (<http://grgs.obs-mip.fr/grace/>).  
240 GRACE  $\Delta$ TWS time-series data have some missing records as the satellites are switched off  
241 for conserving battery life (Shamsudduha *et al.*, 2017); these missing records are linearly  
242 interpolated (Shamsudduha *et al.*, 2012).

243

244 To derive  $\Delta$ GWS from GRACE  $\Delta$ TWS (eq. 1) we use simulated soil moisture to represent  
245  $\Delta$ SMS and surface runoff, as a proxy for  $\Delta$ SWS (Mishra *et al.*, 2016), from LSMs within  
246 NASA's Global Land Data Assimilation System (GLDAS). We apply monthly  $\Delta$ SMS and  
247 surface runoff data at a spatial resolution of  $1^\circ \times 1^\circ$  from 4 GLDAS LSMs: The Community  
248 Land Model (CLM, version 2) (Dai *et al.*, 2003), NOAH (version 2.7.1) (Ek *et al.*, 2003), the  
249 Variable Infiltration Capacity (VIC) model (version 1.0) (Liang *et al.*, 2003), and MOSAIC  
250 Mosaic (version 1.0) (Koster and Suarez, 1992). The respective total depths of modelled soil  
251 profiles are 3.4 m, 2.0 m, and 1.9 m and 3.5 m in CLM (10 vertical layers), NOAH (4 vertical  
252 layers), and VIC (3 vertical layers), and Mosaic (3 vertical layers) (Rodell *et al.*, 2004). In the  
253 absence of in situ  $\Delta$ SMS and  $\Delta$ SWS data in the study areas, we apply an ensemble mean of the  
254 4 LSMs-derived  $\Delta$ SMS and  $\Delta$ SWS data in order to disaggregate GRACE  $\Delta$ TWS signals across  
255 our study regions, for the period August 2002 to July 2016, similar to the approach applied for  
256 other locations by Shamsudduha *et al.* (2012, 2017). To help interpretation of these mean

257  $\Delta$ GWS signals we also present the total uncertainty in estimates of  $\Delta$ GWS which result from  
258 the uncertainty in estimates of  $\Delta$ TWS,  $\Delta$ SMS and  $\Delta$ SWS (blue shading in Fig. 5(c)). The  
259 uncertainty in these individual water balance components is shown in Fig. S2 i.e. the range in  
260 estimated GRACE  $\Delta$ TWS across the three retrieval estimates, and the ranges in estimates  
261  $\Delta$ SMS and  $\Delta$ SWS across the four LSMs. Overall, the total uncertainty in  $\Delta$ GWS can be  
262 substantial and receives roughly equal contribution from uncertainty in  $\Delta$ TWS and  $\Delta$ SMS with  
263 uncertainty in  $\Delta$ SWS important only occasionally. There is some indication that during the  
264 periods of greatest  $\Delta$ GWS uncertainty, the  $\Delta$ TWS uncertainty is most important e.g. 2009-10  
265 and 2015-16 at Limpopo. To understand this uncertainty in GRACE  $\Delta$ TWS further we show  
266 the time series of the three individual  $\Delta$ TWS retrievals of CSR, JPL-Mascons and GRGS (Fig.  
267 S3), which we examine in more detail in Section 3.2.2. For further understanding of the  
268 uncertainty in the estimates water storage from LSMs with respect to GRACE readers are  
269 referred to Scanlon *et al.* (2018).

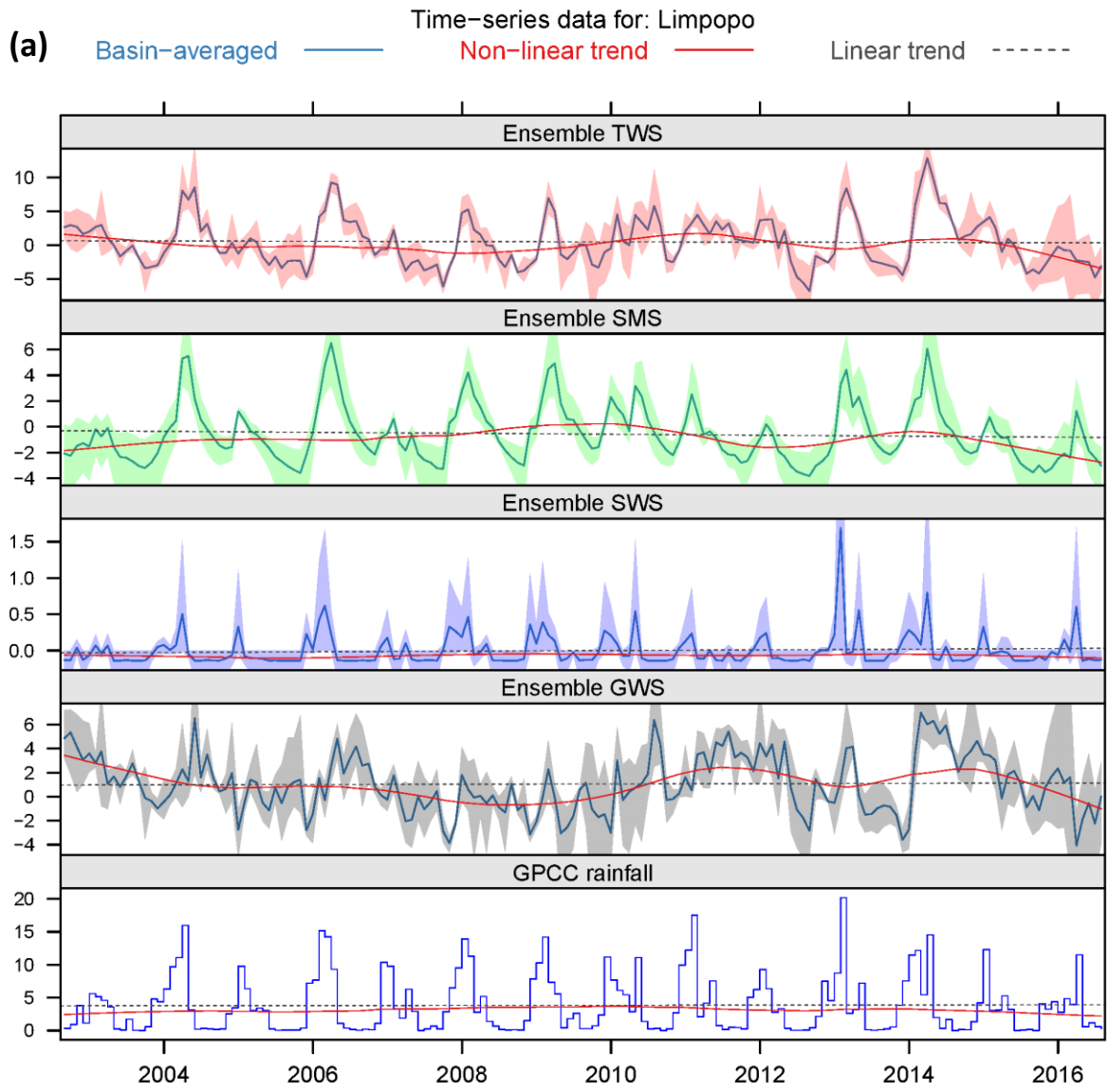


270

271 Fig. S1. (a) Climatological precipitation for the October-April season for the period of 1901-  
 272 2016 ( $\text{mm month}^{-1}$ ). Boxes in Fig. S1(a) show the EASE (small box) and SA (big box) domains  
 273 used in the IAF analysis (see Section 2.1). The blue and red filled circles denote the piezometer  
 274 observation locations at Makutapora, Tanzania and Limpopo, South Africa, respectively. (b)  
 275 Leading mode of interannual October-April variability calculated using the empirical  
 276 orthogonal function (EOF) analysis of de-trended rainfall of GPCP. (c) Correlation between

277 coefficients of EOF1 (Fig. S1(b)) and global SST (October-April mean) 1901-2016. (d) SST  
278 anomalies (K) October-April 2015-16, with respect to 1980-2010 reference period  
279

280  
281  
282  
283  
284  
285  
286  
287  
288  
289  
290  
291  
292  
293  
294  
295  
296  
297  
298  
299  
300  
301  
302  
303  
304  
305  
306  
307  
308



309  
310  
311  
312  
313  
314  
315  
316  
317  
318  
319  
320  
321  
322  
323  
324  
325  
326  
327  
328  
329  
330  
331  
332  
333  
334  
335  
336  
337  
338  
339  
340  
341  
342  
343  
344  
345

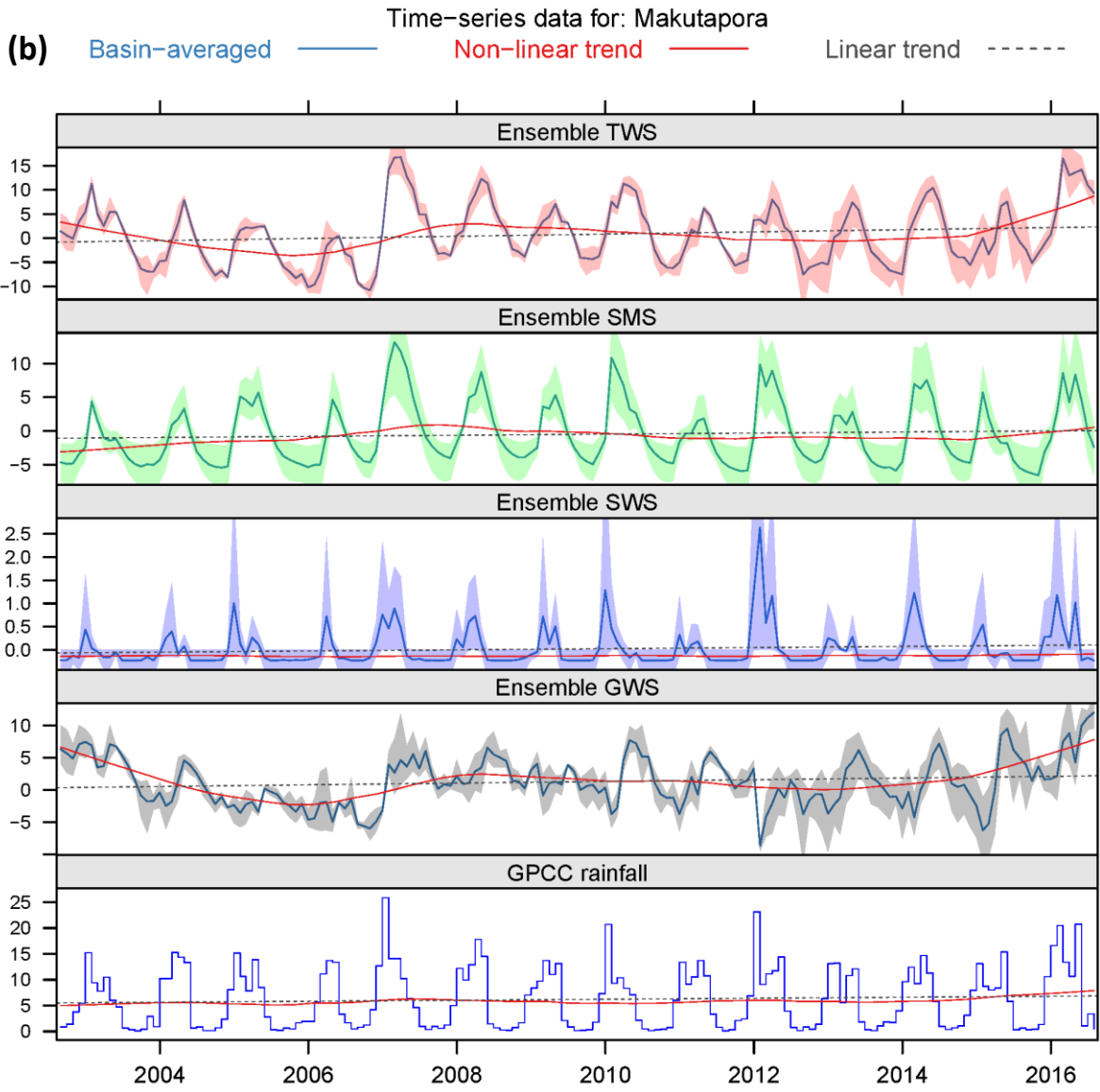
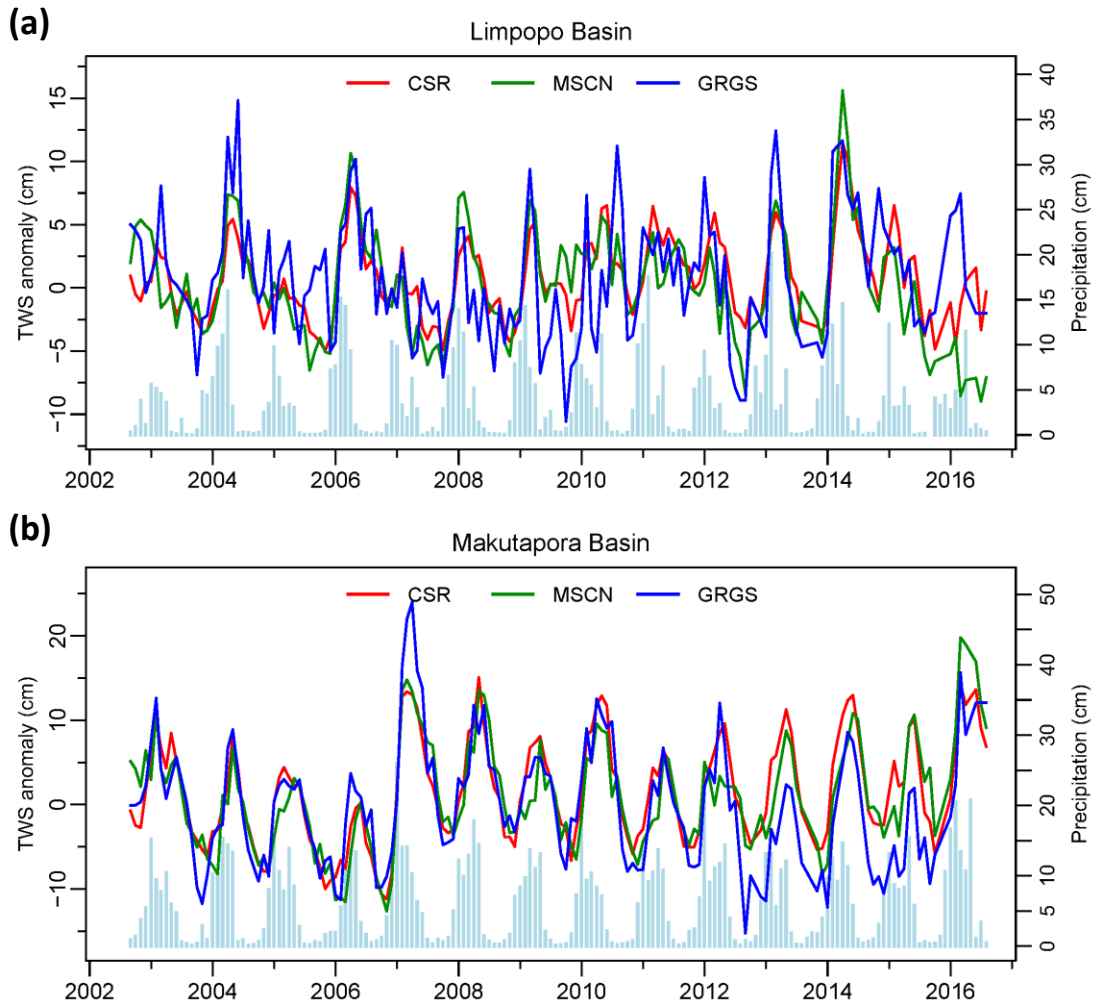


Fig. S2: Time series of monthly estimates of anomalies in the individual components of water balance (lines) and the associated uncertainty range (shaded). From top to bottom TWS from GRACE; SMS and SWS both from LSMs; the residual GWS; observed GPCC rainfall, (all in cm) at (a) Limpopo, and (b) Makutapora.

346  
347  
348  
349  
350  
351  
352  
353  
354  
355  
356  
357  
358  
359  
360  
361  
362  
363  
364  
365  
366  
367  
368  
369  
370



371 Fig. S3: (a) Time series of estimates of monthly  $\Delta$ TWS anomaly (cm) at Limpopo from August  
372 2002 to July 2016 (averaged over an area approximately  $\sim 120\,000\text{ km}^2$ ) derived from the three  
373 individual GRACE retrievals of CSR (red), JPL-Mascons (green) and GRGS (blue). Monthly  
374 rainfall (from GPCP product, cm) shown as bars. (b) As (a) but for Makutapora.

375 **References**

376

377 Allen, M.: Liability for climate change, *Nature*, 421(6926), 891,2003.

378

379 Archer, E. R. M., Landman, W. A., Tadross, M. A., Malherbe, J., Weepener, H., Maluleke,  
380 P., & Marumbwa, F. M.: Understanding the evolution of the 2014–2016 summer rainfall  
381 seasons in southern Africa: Key lessons, *Clim. Risk Manage.*, 16, 22-28, 2017.

382

383 Bindoff, N.L., P.A. Stott, K.M. AchutaRao, M.R. Allen, N. Gillett, D. Gutzler, K. Hansingo,  
384 G. Hegerl, Y. Hu, S. Jain, I.I. Mokhov, J. Overland, J. Perlwitz, R. Sebbari and X. Zhang,:  
385 Detection and Attribution of Climate Change: from Global to Regional. In: Climate Change  
386 2013: The Physical Science Basis. Contribution of Working Group I to the Fifth Assessment  
387 Report of the Intergovernmental Panel on Climate Change [Stocker, T.F., D. Qin, G.-K.  
388 Plattner, M. Tignor, S.K. Allen, J. Boschung, A. Nauels, Y. Xia, V. Bex and P.M. Midgley  
389 (eds.)]. Cambridge University Press, Cambridge, United Kingdom and New York, NY,  
390 USA,2013.

391

392 Berhane, F., & Zaitchik, B: Modulation of daily precipitation over East Africa by the  
393 Madden–Julian oscillation, *J. Climate*, 27(15), 6016-6034, 2014.

394

395 Biancale, R., Lemoine, J-M., Balmino, G., Loyer, S., Bruisma, S., Perosanz, .F, Marty, J-C.,  
396 and Gégout, P.: 3 Years of Geoid Variations from GRACE and LAGEOS Data at 10-day  
397 Intervals from July 2002 to March 2005, CNES/GRGS, 2006

398

399 Black, E., Slingo, J., & Sperber, K. R. :An observational study of the relationship between  
400 excessively strong short rains in coastal East Africa and Indian Ocean SST, *Mon. Weather*  
401 *Rev.*, 131(1), 74-94, 2003.

402

403 Blamey, R. C., Kolusu, S. R., Mahlalela, P., Todd, M. C., & Reason, C. J. C: The role of  
404 regional circulation features in regulating El Niño climate impacts over southern Africa: A  
405 comparison of the 2015/2016 drought with previous events, *Int. J. Climatol.*,,  
406 <https://doi.org/10.1002/joc.5668>, 2018.

407  
408 Coles, S., Bawa, J., Trenner, L., & Dorazio, P.: *An introduction to statistical modelling of*  
409 *extreme values* (Vol. 208), London: Springer, 2001.  
410  
411 Dai, Y., Zeng, X., Dickinson, R. E., Baker, I., Bonan, G. B., Bosilovich, M. G., ... & Oleson,  
412 K. W. :The common land model, *B. Am. Meteorol.*, 84(8), 1013-1024, 2003.  
413  
414 Ek, M. B., Mitchell, K. E., Lin, Y., Rogers, E., Grunmann, P., Koren, V., ... & Tarpley, J. D.  
415 :Implementation of Noah land surface model advances in the National Centers for  
416 Environmental Prediction operational mesoscale Eta model, *J. Geophys. Res.-*  
417 *Atmos.*, 108(D22), 2003.  
418  
419 Goddard, L., & Graham, N. E. :Importance of the Indian Ocean for simulating rainfall  
420 anomalies over eastern and southern Africa, *J. Geophys. Res.-Atmos.*, 104(D16), 19099-  
421 19116, 1999.  
422  
423 Hoell, A., Funk, C., Zinke, J., & Harrison, L.: Modulation of the southern Africa precipitation  
424 response to the El Niño Southern Oscillation by the subtropical Indian Ocean dipole, *Clim.*  
425 *Dynam.*, 48(7-8), 2529-2540, <https://doi.org/10.1007/s00382-016-3220-6>, 2017.  
426  
427 Janowiak, J. E. :An investigation of interannual rainfall variability in Africa. *J. Climate*, 1(3),  
428 240-255, 1988.  
429  
430 Koster, R. D., & Suarez, M. J. : Modeling the land surface boundary in climate models as a  
431 composite of independent vegetation stands, *J. Geophys. Res.-Atmos.*, 97(D3), 2697-2715,  
432 1992.  
433  
434 Landerer, F. W., & Swenson, S. C. :Accuracy of scaled GRACE terrestrial water storage  
435 estimates, *Water Resour. Res.*, 48(4), 2012.  
436  
437 Lazenby, M. J., Todd, M. C., & Wang, Y. : Climate model simulation of the South Indian  
438 Ocean Convergence Zone: mean state and variability, *Clim. Res.*, 68(1), 59-71, 2016.

439  
440 Liang, X., Xie, Z., & Huang, M. :A new parameterization for surface and groundwater  
441 interactions and its impact on water budgets with the variable infiltration capacity (VIC) land  
442 surface model, *J. Geophys. Res.-Atmos.*, 108(D16), 2003.  
443  
444 Lindesay, J. A. : South African rainfall, the Southern Oscillation and a Southern Hemisphere  
445 semi-annual cycle, *J. Climatol.*, 8(1), 17-30, 1988.  
446  
447 Levine, A. F., & McPhaden, M. J.: How the July 2014 easterly wind burst gave the 2015–  
448 2016 El Niño a head start, *Geophys. Res. Lett.*, 43(12), 6503-6510,  
449 <https://doi.org/10.1002/2016GL069204>, 2016.  
450  
451 Manatsa, D., Matarira, C. H., & Mukwada, G.: Relative impacts of ENSO and Indian Ocean  
452 dipole/zonal mode on east SADC rainfall, *Int. J. Climatol.*, 31(4), 558-577, 2011.  
453  
454 Marthews, T. R., Otto, F. E. L., Mitchell, D., Dadson, S. J., & Jones, R. G.: The 2014 drought  
455 in the Horn of Africa: Attribution of meteorological drivers? [in “Explaining Extremes of  
456 2014 from a Climate Perspective”] *B. Am. Meteorol.*, 96(12), S83-S88, 2015.  
457  
458 Mishra, V., & Cherkauer, K. A.: Retrospective droughts in the crop growing season:  
459 Implications to corn and soybean yield in the Midwestern United States, *Agr. Forest*  
460 *Met.*, 150(7-8), 1030-1045, 2010.  
461  
462 Mitchell, D., AchutaRao, K., Allen, M., Bethke, I., Beyerle, U., Ciavarella, A., ... & Ingram,  
463 W. :Half a degree additional warming, prognosis and projected impacts (HAPPI): background  
464 and experimental design, *Geo. Model Develop.*, 10(2), 571-583, [https://doi.org/10.5194/gmd-](https://doi.org/10.5194/gmd-10-571-2017)  
465 [10-571-2017](https://doi.org/10.5194/gmd-10-571-2017), 2017.  
466  
467 Nicholson, S. E.: Climate and climatic variability of rainfall over eastern Africa, *Rev.*  
468 *Geophys.*, 55(3), 590-635, 2017.

469 Philip, S., Kew, S. F., Jan van Oldenborgh, G., Otto, F., O’Keefe, S., Hausteine, K., ... &  
470 Singh, R. Attribution analysis of the Ethiopian drought of 2015, *J. Climate*, 31(6), 2465-  
471 2486, 2018.

472

473 Preethi, B., Sabin, T. P., Adedoyin, J. A., & Ashok, K.: Impacts of the ENSO Modoki and  
474 other tropical Indo-Pacific climate-drivers on African rainfall, *Sci. Rep.*, 5, 16653, 2015.

475

476 Ratnam, J. V., Behera, S. K., Masumoto, Y., & Yamagata, T. :Remote effects of El Niño and  
477 Modoki events on the austral summer precipitation of southern Africa, *J. Climate*, 27(10),  
478 3802-3815, 2014.

479

480 Reason, C. J. C., Allan, R. J., Lindesay, J. A., & Ansell, T. J. : ENSO and climatic signals  
481 across the Indian Ocean basin in the global context: Part I, Interannual composite  
482 patterns. *International J. Climatol.*, 20(11), 1285-1327, 2000.

483

484 Reason, C. J. C. : Subtropical Indian Ocean SST dipole events and southern African  
485 rainfall, *Geophys. Res. Lett.*, 28(11), 2225-2227, 2001

486

487 Robeson, S. M. :Revisiting the recent California drought as an extreme value, *Geophys. Res.*  
488 *Lett.*, 42(16), 6771-6779, 2015.

489

490 Rodell, M., Houser, P. R., Jambor, U. E. A., Gottschalck, J., Mitchell, K., Meng, C. J., ... &  
491 Entin, J. K. ;The global land data assimilation system, *B. Am. Meteorol.*, 85(3), 381-394,  
492 2004.

493

494 Ropelewski, C. F., & Halpert, M. S. : Global and regional scale precipitation patterns  
495 associated with the El Niño/Southern Oscillation. *Mon. Weather Rev.*, 115(8), 1606-1626,  
496 1987.

497

498 SADC 2016a: SADC regional situation update on El Nino-induced drought, Issue 02, 12th  
499 September 2016, SADC, 12pp, available at:

500 ,[https://www.sadc.int/files/9514/7403/9132/SADC\\_Regional\\_Situation\\_Update\\_No-2\\_16-](https://www.sadc.int/files/9514/7403/9132/SADC_Regional_Situation_Update_No-2_16-)  
501 09-2016.pdf, 2016.

502

503 SADC 2016b: SADC Regional Vulnerability Assessment and Analysis Synthesis Report:  
504 State of Food Insecurity and Vulnerability in the Southern African Development Community,  
505 SADC, 66pp, available at: [https://www.sadc.int/files/9014/7911/5767/SADC\\_RVAA-](https://www.sadc.int/files/9014/7911/5767/SADC_RVAA-)  
506 [August-Final-Web.pdf](https://www.sadc.int/files/9014/7911/5767/SADC_RVAA-August-Final-Web.pdf), 2016

507

508 Saji, N. H., Goswami, B. N., Vinayachandran, P. N., & Yamagata, T.: A dipole mode in the  
509 tropical Indian Ocean, *Nature*, 401(6751), 360, doi:10.1038/43854, 1999.

510

511 Scanlon, B. R., Longuevergne, L. , and Long, D.: Ground referencing GRACE satellite  
512 estimates of groundwater storage changes in the California Central Valley, USA *Water*  
513 *Resour. Res.*, 48 W04520, 2012.

514

515 Scanlon, B. R., Zhang, Z., Save, H., Sun, A. Y., Schmied, H. M., van Beek, L. P., ... &  
516 Longuevergne, L. : Global models underestimate large decadal declining and rising water  
517 storage trends relative to GRACE satellite data, *P. Nat. Acad. Sci*, 201704665,  
518 <https://doi.org/10.1073/pnas.1704665115>, 2018.

519

520 Shamsudduha, M., Taylor, R. G., & Longuevergne, L.: Monitoring groundwater storage  
521 changes in the highly seasonal humid tropics: Validation of GRACE measurements in the  
522 Bengal Basin, *Water Resour. Res.*, 48(2), 2012.

523

524 Shamsudduha, M., Taylor, R. G., Jones, D., Longuevergne, L., Owor, M., & Tindimugaya, C.  
525 :Recent changes in terrestrial water storage in the Upper Nile Basin: an evaluation of  
526 commonly used gridded GRACE products, *Hydrol. Earth Syst. Sci.*, 21(9), 4533-4549,  
527 <https://doi.org/10.5194/hess-21-4533-2017>, 2017.

528

529 Siderius, C., Gannon, K. E., Ndiyoi, M., Opere, A., Batisani, N., Olago, D., ... & Conway, D.  
530 :Hydrological response and complex impact pathways of the 2015/2016 El Niño in Eastern  
531 and Southern Africa, *Earth's Fut.*, 6(1), doi:10.1002/2017EF000680,2-22, 2018.

532  
533 Stott, P. A., Hegerl, G. C., Herring, S. C., Hoerling, M .P., Peterson, T. C., Zhang, X., and  
534 Zwiers, F. W.: Introduction to explaining extreme events of 2013 from a climate perspective,  
535 *B. Am. Meteorol.*, 95 S1–S3, 2014  
536  
537 Swenson, S., & Wahr, J.: Post-processing removal of correlated errors in GRACE  
538 data, *Geophys. Res. Lett.*, 33(8), 2006.  
539  
540 Taylor, R. G., Todd, M. C., Kongola, L., Maurice, L., Nahozya, E., Sanga, H., & MacDonald,  
541 A. M. : Evidence of the dependence of groundwater resources on extreme rainfall in East  
542 Africa, *Nature Clim. Cha.*, 3(4), 374, 2013.  
543  
544 Vicente-Serrano, S. M., Beguería, S., & López-Moreno, J. I. : A multiscalar drought index  
545 sensitive to global warming: the standardized precipitation evapotranspiration index, *J.*  
546 *Climate*, 23(7), 1696-1718, 2010.  
547  
548 Watkins, M. M., Wiese, D. N., Yuan, D. N., Boening, C., & Landerer, F. W. : Improved  
549 methods for observing Earth's time variable mass distribution with GRACE using spherical  
550 cap mascons, *J. Geo. Res.: Solid Earth*, 120(4), 2648-2671, 2015.  
551  
552 Wiese, D. N., Yuan, D-N., Boening, C., Landerer, F. W., and Watkins, M. M.: JPL GRACE  
553 Mascon Ocean, Ice, and Hydrology Equivalent Water Height JPL RL05M.1. Ver. 1  
554 PO.DAAC CA USA, 2015.  
555  
556 Wiese, D. N., Landerer, F. W., and Watkins, M. M.: Quantifying and reducing leakage errors  
557 in the JPL RL05M GRACE mascon solution, *Water Resour.Res.*, 52, 7490-7502, 2016.